Journal of
Marine Science and Engineering

Article

The Depth Distribution Law of the Polarization of the Vector Acoustic Field in the Ocean Waveguide

Yizheng Wei [1,2] **and Chao Sun** [1,2,*]

[1] School of Marine Science and Technology, Northwestern Polytechnical University, Xi'an 710072, China; yzwei@mail.nwpu.edu.cn
[2] Key Laboratory of Ocean Acoustic and Sensing, Ministry of Industry and Information Technology, Northwestern Polytechnical University, Xi'an 710072, China
* Correspondence: csun@nwpu.edu.cn

Abstract: The polarization of the acoustic field in the ocean waveguide environment is a unique property that can provide new ideas for locating and detecting the underwater target, so it is interesting to study the polarization. This paper extends the Stokes parameters to a broadband form, and uses the non-stationary phase approximation method to simplify the expressions, reducing the complexity of theoretical derivation. A physical phenomenon is observed where polarization exhibits significant variations concerning the sea surface, seafloor, source depth, and the source symmetrical depth. Simulation results demonstrate that the simplified equations using the non-stationary phase approximation are effective. Additionally, by normalizing the broadband Stokes parameters, the effects of horizontal range on the depth distribution law of polarization can be eliminated. Subsequently, using the normalized broadband Stokes parameters, the influence of environmental and source parameters on the depth distribution law of polarization is analyzed. The effectiveness of the non-stationary phase approximation and the range-independence property of the normalized broadband Stokes parameters are verified by processing RHUM-RUM experimental data. Based on the conclusions of this paper, it is expected that the polarization can be used for target depth estimation.

Keywords: polarization; vector acoustic field; shallow sea; Stokes parameters

Citation: Wei, Y.; Sun, C. The Depth Distribution Law of the Polarization of the Vector Acoustic Field in the Ocean Waveguide. *J. Mar. Sci. Eng.* **2024**, *12*, 1325. https://doi.org/10.3390/jmse12081325

Academic Editor: Lei Wan

Received: 19 June 2024
Revised: 3 August 2024
Accepted: 4 August 2024
Published: 5 August 2024

1. Introduction

Polarization refers to the phenomenon where the vibration vector of a transverse wave at a specific location, within a plane perpendicular to the propagation direction of the wave, varies with time. The path of the endpoint of the vibration vector can be a straight line, circle or ellipse, which corresponds to three polarization modes: linear polarization, circular polarization, and elliptical polarization, as shown in Figure 1. Polarization is generally thought not to exist in the acoustic field. As an acoustic plane wave propagates in free space, it exhibits a longitudinal wave nature, characterized by particle velocity oscillating solely along the propagation direction, without any rotational motion. However, researchers have discovered that when two plane waves interfere, the particle velocity vectors in the acoustic field rotate. Long et al. found that, for the combinations of two longitudinal waves with different wave vectors, the total elastic field carries nontrivial spin angular momentum density due to the wave interference related to the rotation of the vector field [1]. Shi et al., through experimental observations, demonstrated that when two plane waves with orthogonal propagation directions, different phases and identical frequencies interfere, the particle velocity vector undergoes rotation, providing evidence for the existence of polarization in the acoustic field [2]. Li et al. proposed using the curl of the active sound intensity to estimate the polarization law of the acoustic field [3]. Building upon this foundation, scholars have extensively researched the properties and applications of spin angular momentum in the acoustic field [4–6].

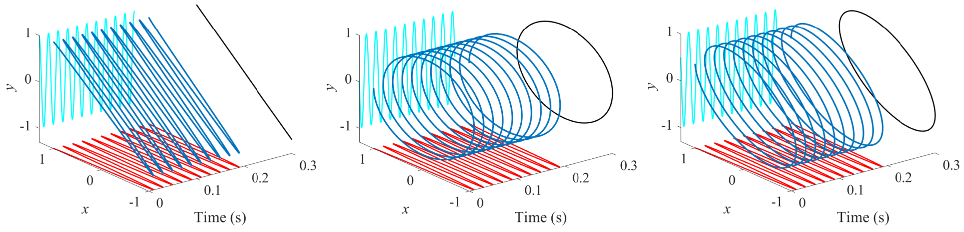

(**a**) (**b**) (**c**)

Figure 1. Polarization of transverse wave: (**a**) linear polarization, (**b**) circular polarization, and (**c**) elliptical polarization.

Based on the findings of the aforementioned research, it can be concluded that the essence of polarization of the acoustic field lies in the rotation of particle velocity. In the field of underwater acoustics, scholars have also investigated the rotational characteristics of vector acoustic field. Shchurov observed the rotational nature of the acoustic energy flux through a sea trial [7]. D'Spain and Hodgkiss discussed the relationship between the cross-spectral matrix of particle velocity, acoustic energy flux, and polarization in the oceanic acoustic field [8]. Dall'Osto and Dahl pointed out that the multipath interference of sound waves in shallow water waveguide causes elliptical motion of the particle and proposed the use of circularity to describe the particle's path [9]. Then, they utilized the circularity of the acoustic field radiated from explosion sources [10] and ship noise [11] for geoacoustic inversion. Liu proposed a direction-of-arrival (DOA) estimation method for underwater targets based on the polarization characteristic of vector signal field [12]. Bonnel et al. [13], combining the Stokes parameters [14] with normal mode theory, derived theoretical expressions for the vector acoustic field's Stokes parameters. Then, Dahl et al. pointed out that polarization characteristics can be utilized for source localization [15], and further studied the properties of active intensity vortex in shallow-water waveguide using circularity [16]. Polarization holds significant application potential in underwater acoustics. However, there is currently limited research on the polarization of underwater acoustics. Therefore, researching the polarization of underwater acoustics is meaningful.

In the existing research, Stokes parameters of the vector acoustic field proposed by Bonnel et al. provide a comprehensive description of the polarization of underwater acoustics. However, the complex cross terms in the expressions present challenges for further investigation. To address this, this paper extends Stokes parameters of the vector acoustic field to a broadband form, and uses the non-stationary phase approximation to eliminate the influence of cross terms, thus avoiding the complexity introduced by these terms. The depth distribution law of the broadband Stokes parameters in an ideal environment are derived, revealing the underlying physical mechanisms. The depth distribution of the broadband Stokes parameters in the Pekeris waveguide are also studied through simulations. Furthermore, using the normalized broadband Stokes parameters as the research focus, this study analyzes the influence of environmental and source parameters on the polarization depth distribution law in shallow water.

This paper is organized as follows. Section 2 introduces the broadband Stokes parameters. Section 3 analyzes the depth distribution law of polarization in an ideal environment. Section 4 conducts a simulation, and Section 5 processes the RHUM-RUM experimental data to validate the law. The conclusion is presented in Section 6.

2. The Polarization of the Vector Acoustic Field

2.1. Polarization

According to reference [17], we assume a plane wave propagates in the acoustic field, the two orthogonal components of the particle velocity vector at a fixed position can be expressed as:

$$\begin{aligned} v_x &= a \cdot \cos\alpha \cdot \sin(\omega t) \\ v_y &= a \cdot \sin\alpha \cdot \sin(\omega t), \end{aligned} \tag{1}$$

where a represents the amplitude of the wave, α denotes the direction of wave propagation. By simultaneously solving the two equations and eliminating t, we obtain:

$$\begin{aligned} \left(\frac{v_x}{a\cos\alpha}\right)^2 + \left(\frac{v_y}{a\sin\alpha}\right)^2 - 2\frac{v_x v_y}{a^2\cos\alpha\sin\alpha} &= 0 \\ \frac{v_y}{v_x} &= \tan\alpha, \end{aligned} \tag{2}$$

this is a linear equation, indicating that the particle velocity vector oscillates along a straight line.

In the case of interference between two plane waves,

$$\begin{aligned} v_x &= a \cdot \cos\alpha \cdot \sin(\omega t) + b \cdot \cos\beta \cdot \sin(\omega t + \delta) = q_x \cdot \sin(\omega t + \delta_x) \\ v_y &= a \cdot \sin\alpha \cdot \sin(\omega t) + b \cdot \sin\beta \cdot \sin(\omega t + \delta) = q_y \cdot \sin(\omega t + \delta_y), \end{aligned} \tag{3}$$

where

$$q_x = \sqrt{(a\cos\alpha + b\cos\beta\cos\delta)^2 + (b\cos\beta\sin\delta)^2}, \tag{4}$$

$$q_y = \sqrt{(a\sin\alpha + b\sin\beta\cos\delta)^2 + (b\sin\beta\sin\delta)^2}, \tag{5}$$

$$\delta_x = \arctan\frac{b\cos\beta\sin\delta}{a\cos\alpha + b\cos\beta\cos\delta}, \tag{6}$$

$$\delta_y = \arctan\frac{b\sin\beta\sin\delta}{a\sin\alpha + b\sin\beta\cos\delta}. \tag{7}$$

The equation of motion for the particle velocity vector is

$$\left(\frac{v_x}{q_x}\right)^2 + \left(\frac{v_y}{q_y}\right)^2 - 2\frac{v_x}{q_x}\frac{v_y}{q_y}\cos(\delta_y - \delta_x) = \sin^2(\delta_y - \delta_x). \tag{8}$$

It can be observed that this is an elliptical equation, indicating that the endpoint trajectory of the particle velocity vector forms an ellipse, resulting in the rotation of the particle velocity vector. This phenomenon is called the polarization of the acoustic field. Simultaneously, we can understand that the amplitude and phase difference of the two orthogonal components of the velocity vector determine the polarization.

2.2. Stokes Parameters

In optics, Stokes parameters are commonly used to describe polarization. Stokes parameters consist of four parameters: S_0 represents total intensity, S_1, S_2, and S_3 give the geometric polarization properties. In the realm of acoustics, Bonnel decomposed the particle velocity into horizontal component v_r and vertical component v_z, utilizing this model to elucidate polarization. This framework can characterize the amplitude and phase relationship between the particle velocity components [13]:

$$\begin{aligned} S_0(f) &= |v_r(f)|^2 + |v_z(f)|^2 \\ S_1(f) &= |v_r(f)|^2 - |v_z(f)|^2 \\ S_2(f) &= 2\mathrm{Re}[v_r(f)v_z^*(f)] \\ S_3(f) &= 2\mathrm{Im}[v_r(f)v_z^*(f)], \end{aligned} \tag{9}$$

where S_0 represents the total kinetic energy of the sound wave. S_1 represents the energy difference between the horizontal and vertical components of the particle velocity, indicating the linear polarization component of the sound wave in the horizontal direction.

S_2 represents the linear polarization component of the sound wave in the 45° direction. S_3 represents the circular polarization component of the sound wave. When $S_3 = \pm S_0$, it denotes a fully circular polarization state. If $S_3 > 0$, the polarization ellipse rotates counterclockwise. Figure 2 illustrates the particle's elliptical trajectory, with the association between the four Stokes parameters and the elliptical path outlined as follows:

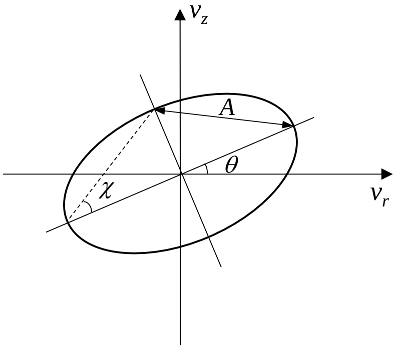

Figure 2. Elliptical path of acoustic particle motion.

$$\begin{aligned} A &= S_0 \\ S_1 &= S_0 \cos 2\chi \cos 2\theta \\ S_2 &= S_0 \cos 2\chi \sin 2\theta \\ S_3 &= S_0 \sin 2\chi. \end{aligned} \tag{10}$$

where A represents the size of the ellipse, θ represents the angle between the major axis of the ellipse and the horizontal direction, and χ is the ellipticity angle, representing the shape and the rotation direction of the ellipse. Dividing S_1, S_2, and S_3 by S_0 yields the normalized Stokes parameters:

$$s_1 = \frac{S_1}{S_0}, \quad s_2 = \frac{S_2}{S_0}, \quad s_3 = \frac{S_3}{S_0}. \tag{11}$$

The normalized Stokes parameters remove the influence of energy on the polarization state, retaining only the geometric polarization properties.

2.3. Model for Polarization Based on Normal Mode Theory

In the ocean waveguide, the acoustic field comprises the interference between the source signal and its reflections, indicating the presence of polarization in the acoustic field. There are several theories available for computing the acoustic field in an ocean waveguide, such as normal mode theory and ray theory. This research primarily concentrates on the low-frequency and far-field scenarios, leading us to utilize normal mode theory to model the acoustic field in the ocean waveguide.

According to reference [18] (pp. 267–269), the sound pressure in the waveguide can be expressed as the sum of a series of normal modes. In a horizontally stratified medium with water depth H, where the underwater source is at range r and received at depth z, the expression for the received pressure in normal mode can be stated as:

$$p(r,z,f) = \Omega(f) \frac{ie^{-i\frac{\pi}{4}}}{\rho(z_s)\sqrt{8\pi r}} \sum_{n=1}^{N} \varphi_n(z_s)\varphi_n(z) \frac{1}{\sqrt{k_{rn}}} e^{ik_{rn}r}, \tag{12}$$

where f is frequency, $\Omega(f)$ is the spectrum of source signal, N is the number of propagating modes, z_s is the depth of source, $\rho(z_s)$ is the density at source depth, $\varphi_n(z)$ and k_{rn} are the modal function and the horizontal wavenumber of n-*th* mode, respectively.

Newton's second law establishes a connection between the sound pressure $p(r,z)$ and the particle velocity $\mathbf{v}(r,z)$ in the acoustic field as follows:

$$\mathbf{v}(r,z) = \frac{i}{\rho(z_s)\omega} \cdot \nabla p(r,z), \tag{13}$$

where $\omega = 2\pi f$. By substituting Equation (12) into (13), the expressions for the horizontal and vertical particle velocities can be obtained as follows:

$$v_r(r,z,f) = \Omega(f)\frac{ie^{-i\frac{\pi}{4}}}{\rho^2(z_s)\omega\sqrt{8\pi r}}\sum_{n=1}^{N}\varphi_n(z_s)\varphi_n(z)\sqrt{k_{rn}}e^{ik_{rn}r}, \tag{14}$$

$$v_z(r,z,f) = \Omega(f)\frac{e^{-i\frac{\pi}{4}}}{\rho^2(z_s)\omega\sqrt{8\pi r}}\sum_{n=1}^{N}\varphi_n(z_s)\varphi_n'(z)\frac{e^{ik_{rn}r}}{\sqrt{k_{rn}}}, \tag{15}$$

where ${\varphi'}_n(z) = \partial\varphi_n(z)/\partial z$ represents the partial derivative of the modal depth function of n-th mode with respect to the depth.

By substituting Equations (14) and (15) into Equation (9), the expressions for the Stokes parameters can be written as

$$\begin{aligned}
S_0 =&|v_r|^2 + |v_z|^2\\
=&\frac{|Q(f)|^2}{r}\left(\sum_{n=1}^{N}\varphi_n^2(z_s,f)\left[\varphi_n^2(z,f)k_{rn}(f) + \frac{{\varphi'}_n^2(z,f)}{k_{rn}(f)}\right]\right.\\
&+\sum_{\substack{n,m=1\\n\neq m}}^{N}\varphi_n(z_s,f)\varphi_m(z_s,f)\varphi_n(z,f)\varphi_m(z,f)\sqrt{k_{rn}(f)k_{rm}(f)}e^{i\Delta k_{nm}(f)r}\\
&\left.+\sum_{\substack{n,m=1\\n\neq m}}^{N}\varphi_n(z_s,f)\varphi_m(z_s,f){\varphi'}_n(z,f){\varphi'}_m(z,f)\frac{e^{i\Delta k_{nm}(f)r}}{\sqrt{k_{rn}(f)k_{rm}(f)}}\right)\\
=&\sum_{n=1}^{N}I_{S_0,n}(z) + \sum_{\substack{n,m=1\\n\neq m}}^{N}J_{S_0,nm}(z),
\end{aligned} \tag{16}$$

$$\begin{aligned}
S_1 =&|v_r|^2 - |v_z|^2\\
=&\frac{|Q(f)|^2}{r}\left(\sum_{n=1}^{N}\varphi_n^2(z_s,f)\left[\varphi_n^2(z,f)k_{rn}(f) - \frac{{\varphi'}_n^2(z,f)}{k_{rn}(f)}\right]\right.\\
&+\sum_{\substack{n,m=1\\n\neq m}}^{N}\varphi_n(z_s,f)\varphi_m(z_s,f)\varphi_n(z,f)\varphi_m(z,f)\sqrt{k_{rn}(f)k_{rm}(f)}e^{i\Delta k_{nm}(f)r}\\
&\left.-\sum_{\substack{n,m=1\\n\neq m}}^{N}\varphi_n(z_s,f)\varphi_m(z_s,f){\varphi'}_n(z,f){\varphi'}_m(z,f)\frac{e^{i\Delta k_{nm}(f)r}}{\sqrt{k_{rn}(f)k_{rm}(f)}}\right)\\
=&\sum_{n=1}^{N}I_{S_1,n}(z) + \sum_{\substack{n,m=1\\n\neq m}}^{N}J_{S_1,nm}(z),
\end{aligned} \tag{17}$$

$$\begin{aligned}
S_2 =&2\cdot\mathrm{Re}(v_r v_z^*)\\
=&2\frac{|Q(f)|^2}{r}\sum_{\substack{n,m=1\\n\neq m}}^{N}\varphi_n(z_s,f)\varphi_m(z_s,f)\varphi_n(z,f){\varphi'}_m(z,f)\sqrt{\frac{k_{rn}(f)}{k_{rm}(f)}}\sin(\Delta k_{nm}(f)r)\\
=&\sum_{\substack{n,m=1\\n\neq m}}^{N}J_{S_2,nm}(z),
\end{aligned} \tag{18}$$

$$
\begin{aligned}
S_3 =& 2 \cdot \mathrm{Im}(v_r v_z^*) \\
=& 2\frac{|Q(f)|^2}{r}\left(\sum_{n}^{N} \varphi_n^2(z_s,f)\varphi_n(z,f)\varphi'_n(z,f)\right. \\
&\left. + \sum_{\substack{n,m=1 \\ n\neq m}}^{N} \varphi_n(z_s,f)\varphi_m(z_s,f)\varphi_n(z,f)\varphi'_m(z,f)\sqrt{\frac{k_{rn}(f)}{k_{rm}(f)}}\cos(\Delta k_{nm}(f)r)\right) \\
=& \sum_{n=1}^{N} I_{S_3,n}(z) + \sum_{\substack{n,m=1 \\ n\neq m}}^{N} J_{S_3,nm}(z),
\end{aligned}
\tag{19}
$$

where $Q(f) = \Omega(f)\frac{e^{-i\frac{\pi}{4}}}{\rho^2(z_s)\omega\sqrt{8\pi}}$, $I_{S_k,n}(k = 0,1,2,3)$ represents an incoherent term and $J_{S_k,nm}$, $(k = 0,1,2,3)$ is a coherent cross term. Equations (16)–(19) demonstrate that the Stokes parameters consist of two components. For the single-frequency case, it can be observed that the sum of cross term $\sum_{\substack{n,m=1 \\ n\neq m}}^{N} J_{S_k,nm}$ is highly complex, and its complexity increases with the number of modes, making it difficult to extract law. As indicated in reference [19], broadening the Stokes parameters into a broadband format helps alleviate the impact of cross terms.

For a broadband signal, the broadband Stokes parameters are defined as follows:

$$
S_0^{[f_1,f_2]}(z) \triangleq \int_{f_1}^{f_2} S_0(f,z)df, \tag{20}
$$

$$
S_1^{[f_1,f_2]}(z) \triangleq \int_{f_1}^{f_2} S_1(f,z)df, \tag{21}
$$

$$
S_2^{[f_1,f_2]}(z) \triangleq \int_{f_1}^{f_2} S_2(f,z)df, \tag{22}
$$

$$
S_3^{[f_1,f_2]}(z) \triangleq \int_{f_1}^{f_2} S_3(f,z)df. \tag{23}
$$

The broadband Stokes parameters can also be divided into two parts:

$$
S_k^{[f_1,f_2]}(z) = \sum_{n=1}^{N} I_{S_k,n}^{[f_1,f_2]}(z) + \sum_{\substack{n,m=1 \\ n\neq m}}^{N} J_{S_k,nm}^{[f_1,f_2]}(z), k = 0,1,2,3. \tag{24}
$$

From Equation (24), it can be observed that the cross terms of the broadband Stokes parameters are still complex, which hinders the analysis of the properties of the broadband Stokes parameters. Hence, a need for additional simplification arises. Reference [19] illustrates that by fulfilling the following assumptions:

1. The bandwidth of the source signal is limited, $\Omega(f) = 0$, when $f \notin [f_1, f_2]$ or f_1 is lower than the cutoff frequency of the waveguide;
2. The group velocities of different modes within the frequency band do not intersect, or the intersection of group velocities occurs near the Airy phase. This assumption is easily met in a relatively simple shallow water waveguide. In the deep sea, it holds true only in scenarios near the seabed with low processing frequency, as detailed in Section 5. This is a primary reason for the selection of a shallow water environment in this study.

Then we can use non-stationary phase principle to integral $J_{k,nm}^{[f_1,f_2]}$, when $r \to \infty$, $J_{k,nm}^{[f_1,f_2]}(z) \to 0$.

Therefore, In the case of $r \gg 1$, the broadband Stokes parameters can be approximated as

$$S_0^{[f_1,f_2]}(z) \approx \sum_{n=1}^{N} I_{S_0,n}^{[f_1,f_2]}(z), \tag{25}$$

$$S_1^{[f_1,f_2]}(z) \approx \sum_{n=1}^{N} I_{S_1,n}^{[f_1,f_2]}(z), \tag{26}$$

$$S_2^{[f_1,f_2]}(z) \approx 0, \tag{27}$$

$$S_3^{[f_1,f_2]}(z) \approx \sum_{n=1}^{N} I_{S_3,n}^{[f_1,f_2]}(z). \tag{28}$$

Because $S_2^{[f_1,f_2]}(z)$ does not include incoherent terms, $S_2^{[f_1,f_2]}(z) \approx 0$, which indicates that the polarization state at each depth in the acoustic field is hardly influenced by linear polarization component along the 45° direction. The polarization state at each depth is determined only by the horizontal linear and circular polarization components.

3. The Depth Distribution Law of Polarization of the Vector Acoustic Field

According to reference [18] (pp. 272–275), in an ideal isovelocity waveguide with a solid seafloor, it is established that the modal depth function and vertical wavenumber remain frequency-independent. The expressions is as follows:

$$\varphi_n(z) = \sqrt{\frac{2\rho_0}{H}} \sin k_{zn} z, \quad k_{zn} = \frac{\pi}{H}\left(n - \frac{1}{2}\right), \tag{29}$$

where ρ_0 represents the density of water column, H is the water depth, k_{zn} is the vertical wavenumber, $k_{zn}^2 = \omega^2/c^2 - k_{rn}^2$. Plugging Equation (29) into (25), Equation (25) can be rewritten as

$$\begin{aligned} I_{S_0,n}^{[f_1,f_2]}(z) &= \frac{1}{r}\int_{f_1}^{f_2} \frac{|Q(f)|^2}{k_{rn}(f)} \frac{4\rho_0^2}{H^2} \sin^2(k_{zn}z_s)\left[\sin^2(k_{zn}z)k_{rn}^2(f) + \cos^2(k_{zn}z)k_{zn}^2\right]df \\ &= \frac{1}{r}\int_{f_1}^{f_2} \frac{|Q(f)|^2}{k_{rn}(f)} \frac{4\rho_0^2}{H^2} \sin^2(k_{zn}z_s)\left[\sin^2(k_{zn}z)\left(\frac{\omega^2}{c^2} - 2k_{zn}^2\right) + k_{zn}^2\right]df \\ &= \frac{1}{r}\left[a_n^{[f_1,f_2]}\sin^2(k_{zn}z_s)\sin^2(k_{zn}z) + g_n\right], \end{aligned} \tag{30}$$

where

$$a_n^{[f_1,f_2]} = \int_{f_1}^{f_2} \frac{|Q(f)|^2}{k_{rn}(f)} \frac{4\rho_0^2}{H^2}\left(\frac{\omega^2}{c^2} - 2k_{zn}^2\right)df, \tag{31}$$

$$g_n = \int_{f_1}^{f_2} \frac{|Q(f)|^2}{k_{rn}(f)} \frac{4\rho_0^2}{H^2} k_{zn}^2 df. \tag{32}$$

The second term on the right side of Equation (30) is solely frequency-dependent and not influenced by depth. The depth dependence of $I_{S_0,n}^{[f_1,f_2]}(z)$ is contained within the first term of Equation (30). Simplifying this term leads to

$$\begin{aligned} a_n^{[f_1,f_2]}\sin^2(k_{zn}z_s)\sin^2(k_{zn}z) = & \frac{a_n^{[f_1,f_2]}}{4}\{1 - \cos(2k_{zn}z_s) - \cos(2k_{zn}z) \\ & + \frac{\cos[2k_{zn}(z - z_s)] + \cos[2k_{zn}(z + z_s)]}{2}\Bigg\}. \end{aligned} \tag{33}$$

Substituting Equation (33) into Equation (25) leads to

$$\begin{aligned} S_0^{[f_1,f_2]}(z) &\approx \sum_{n=1}^{N} I_{S_0,n}^{[f_1,f_2]}(z) \\ &= \frac{1}{r}\left\{\frac{1}{4}\left[\sum_{n=1}^{N} a_n^{[f_1,f_2]} - \varepsilon(z_s) - \varepsilon(z) + \frac{\varepsilon(z-z_s)+\varepsilon(z+z_s)}{2}\right] + G\right\}, \end{aligned} \tag{34}$$

where

$$\varepsilon(z) = \sum_{n=1}^{N} a_n^{[f_1,f_2]} \cos(2k_{zn}z), \tag{35}$$

$$G = \sum_{n=1}^{N} g_n. \tag{36}$$

According to reference [19], if the following assumptions are satisfied:

1. f_1 is lower than the cutoff frequency;
2. $f_2 \gg f_1$;
3. The spectrum of source signal is flat, $|\Omega(f)| = 1$ when $f \in [f_1, f_2]$.

Then Equation (35) can be expressed in the form of a convolution between a Dirichlet-like kernel, denoted as $D_N(z)$, and a smoothing operator $A(z)$

$$\varepsilon(z) = (A * D_N)(z), \tag{37}$$

where $*$ represents the convolution operation. The depth dependence of $\varepsilon(z)$ is mainly related to $D_N(z)$:

$$D_N(z) = \sum_{n=1}^{N} \cos(2k_{zn}z) = \cos\left(\frac{\pi}{H}Nz\right)\frac{\sin\left(\frac{\pi}{H}Nz\right)}{\sin\left(\frac{\pi}{H}z\right)}. \tag{38}$$

The properties of $D_N(z)$ are illustrated in Figure 3. At $z = 0$, $D_N(z)$ achieves its maximum value of N, while at $z = H$, it reaches its minimum value of $-N$. Far from these extremes, the amplitude of $D_N(z)$ rapidly diminishes, approaching 0. As $N \to \infty$, $D_N(z) \to \delta(z)$. For $D_N(z+z_s)$, within the interval $[0, H]$, the minimum value is found at $z = H - z_s$. Similarly, for $D_N(z-z_s)$, within the interval $[0, H]$, the maximum value is located at $z = z_s$.

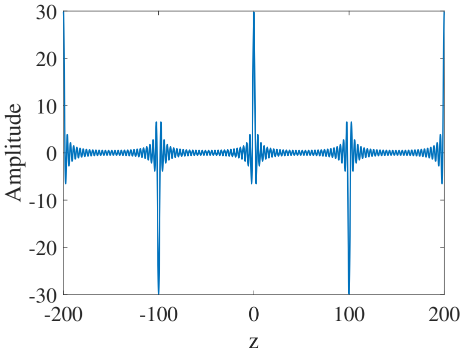

Figure 3. Curve of $D_N(z)$ with z (N = 30, H = 100).

Based on the properties of $D_N(z)$, Equation (34) can be written as

$$\begin{aligned} S_0^{[f_1,f_2]}(z) \approx \frac{1}{r}\Bigg\{\frac{1}{4}\Bigg[&\sum_{n=1}^{N} a_n^{[f_1,f_2]} - (A * D_N)(z_s) - (A * D_N)(z) \\ &+ \frac{(A * D_N)(z-z_s) + (A * D_N)(z+z_s)}{2}\Bigg] + G\Bigg\}. \end{aligned} \tag{39}$$

Equation (39) yields the depth distribution law of $S_0^{[f_1,f_2]}(z)$ as follows: At the sea surface ($z = 0$), the seafloor interface ($z = H$), source depth ($z = z_s$), and symmetric source depth ($z = H - z_s$) exhibit peaks, with peak amplitudes increasing as the number of modes rises. For a sufficiently large N at the sea surface and seafloor interface, $S_0^{[f_1,f_2]}(0) \approx [G - A(0)N/4]/r, \quad S_0^{[f_1,f_2]}(H) \approx [G + A(0)N/4]/r$; at source depth and symmetrical depth, $S_0^{[f_1,f_2]}(z_s) \approx [G + A(0)N/8]/r, \quad S_0^{[f_1,f_2]}(H - z_s) \approx [G - A(0)N/8]/r$.

Similarly, by substituting Equation (29) into Equation (26), we obtain

$$\begin{aligned} I_{S_1,n}^{[f_1,f_2]}(z) &= \frac{1}{r}\int_{f_1}^{f_2} \frac{|Q(f)|^2}{k_{rn}(f)} \frac{4\rho_0^2}{H^2} \sin^2(k_{zn}z_s)\left[\sin^2(k_{zn}z)k_{rn}^2(f) - \cos^2(k_{zn}z)k_{zn}^2\right]df \\ &= \frac{1}{r}\int_{f_1}^{f_2} \frac{|Q(f)|^2}{k_{rn}(f)} \frac{4\rho_0^2}{H^2} \sin^2(k_{zn}z_s)\left[\sin^2(k_{zn}z)\frac{\omega^2}{c^2} - k_{zn}^2\right]df \\ &= \frac{1}{r}\left[b_n^{[f_1,f_2]}\sin^2(k_{zn}z_s)\sin^2(k_{zn}z) - g_n\right], \end{aligned} \tag{40}$$

where

$$b_n^{[f_1,f_2]} = \int_{f_1}^{f_2} \frac{|Q(f)|^2}{k_{rn}(f)} \frac{4\rho_0^2}{H^2} \frac{\omega^2}{c^2} df. \tag{41}$$

Further derivation leads to:

$$\begin{aligned} S_1^{[f_1,f_2]}(z) \approx \frac{1}{r}\Bigg\{\frac{1}{4}\Bigg[&\sum_{n=1}^{N} b_n^{[f_1,f_2]} - (B * D_N)(z_s) - (B * D_N)(z) \\ &+ \frac{(B * D_N)(z - z_s) + (B * D_N)(z + z_s)}{2}\Bigg] - G\Bigg\}. \end{aligned} \tag{42}$$

From Equation (42), it can be seen that the depth distribution law of $S_1^{[f_1,f_2]}(z)$ is similar to $S_0^{[f_1,f_2]}(z)$. Peaks are also present at the sea surface and seafloor interface ($z = 0, z = H$), source depth ($z = z_s$), and source symmetrical depth ($z = H - z_s$). When N is sufficiently large, at the sea surface and seafloor interface, $S_1^{[f_1,f_2]}(0) \approx [-G - B(0)N/4]/r, \quad S_1^{[f_1,f_2]}(H) \approx [-G + B(0)N/4]/r$, at source depth and symmetrical depth $S_1^{[f_1,f_2]}(z_s) \approx [-G + B(0)N/8]/r, \quad S_1^{[f_1,f_2]}(H - z_s) \approx [-G - B(0)N/8]/r$.

By following the same steps, the derivation of Equation (28) yields

$$\begin{aligned} I_{S_3,n}^{[f_1,f_2]}(z) &= \frac{1}{r}\int_{f_1}^{f_2} |Q(f)|^2 \frac{4\rho_0^2}{H^2} \sin^2(k_{zn}z_s) k_{zn} \sin(k_{zn}z)\cos(k_{zn}z) df \\ &= \frac{1}{r} c_n^{[f_1,f_2]} \sin^2(k_{zn}z_s)\sin(2k_{zn}z) \\ &= \frac{c_n^{[f_1,f_2]}}{4r}\{2\sin(2k_{zn}z) - \sin[2k_{zn}(z + z_s)] - \sin[2k_{zn}(z - z_s)]\}. \end{aligned} \tag{43}$$

Equation (43) can be rewritten as

$$S_3^{[f_1,f_2]}(z) \approx \frac{1}{4r}[2(C * E_N)(z) - (C * E_N)(z + z_s) - (C * E_N)(z - z_s)], \tag{44}$$

where

$$E_N(z) = \sum_{n=1}^{N} \sin(2k_{zn}z) = \frac{\sin^2\left(\frac{\pi}{H}Nz\right)}{\sin\left(\frac{\pi}{H}z\right)}. \tag{45}$$

Similarly to $S_0^{[f_1,f_2]}(z)$, the property of $S_3^{[f_1,f_2]}(z)$ is related to E_N. However, the characteristic of E_N is different from D_N, as shown in Figure 4. When $z = nH \quad (n = 0, 1, 2, \ldots)$, $E_N(z) = 0$. Moreover, two peaks with opposite signs are present on either side of the zero point. This information allows us to analyze the depth distribution of $S_3^{[f_1,f_2]}(z)$: at the sea surface and seafloor interface, $S_3^{[f_1,f_2]}(0) = S_3^{[f_1,f_2]}(H) = 0$, yet peaks are in close proximity to these boundaries. At the source depth, $S_3^{[f_1,f_2]}(z_s) = 0$, exhibiting two opposite-signed peaks adjacent to this zero point. Similar phenomena are observed at source symmetrical depth $z = H - z_s$ as well.

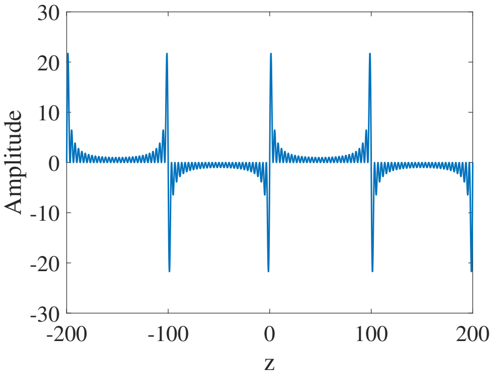

Figure 4. Curve of $E_n(z)$ with z (N = 30, H = 100).

By conducting formula derivation under the assumption of an ideal isovelocity waveguide, we can obtain simple theoretical properties: the polarization of the acoustic field in shallow sea exhibits significant variations at the sea surface, seafloor, source depth, and source symmetrical depth.

According to Equation (11), the normalized broadband Stokes parameters are defined as follows:

$$s_1^{[f_1,f_2]}(z) = \frac{S_1^{[f_1,f_2]}(z)}{S_0^{[f_1,f_2]}(z)}, \quad s_2^{[f_1,f_2]}(z) = \frac{S_2^{[f_1,f_2]}(z)}{S_0^{[f_1,f_2]}(z)}, \quad s_3^{[f_1,f_2]}(z) = \frac{S_3^{[f_1,f_2]}(z)}{S_0^{[f_1,f_2]}(z)}, \tag{46}$$

and after normalization, the range term in the broadband Stokes parameters is eliminated, and the normalized broadband Stokes parameters only capture the depth distribution law of the polarization. This facilitates subsequent simulation studies.

4. Simulation and Discussion

To validate the depth distribution law of the acoustic field's polarization in an ideal isovelocity waveguide environment, and the effectiveness of the non-stationary phase approximation method, this section conducts simulation calculations using KRAKEN software (https://kraken.tech/ 30 April 2024) to investigate the distribution of the broadband Stokes parameters at varying depths. The simulation assumes a water depth of 100 m, a water sound speed of 1500 m/s, and an ideal solid seafloor. The source depth is 25 m, with a lower frequency limit $f_1 = f_{c1}$ and upper frequency limit $f_2 = 250$ Hz; f_{c1} denotes the cutoff frequency, set to 4 Hz in this instance. We set $f_2 = 250$ Hz because within this frequency range, the source can excite a sufficient number of modes, making the depth distribution law of polarization clear enough. The frequency integration step is 0.25 Hz, and the range between receiver and source is 8 km.

Figure 5 gives the broadband Stokes parameters depth distribution curves in an ideal waveguide. The solid blue line denotes the theoretical values calculated using Equation (24), while the dashed red line represents the approximated values derived from Equations (25)–(28) and the solid black line represents the source depth and symmetrical depth. The close alignment between theoretical and approximated values confirms the efficacy of the non-stationary phase approximation. Furthermore, the observed variation in the broadband Stokes parameters varying with depth in the graph aligns with that derived in the previous section; $S_0^{[f_1,f_2]}$ and $S_1^{[f_1,f_2]}$ have similar trends. The minimum and maximum values occur, respectively, at the sea surface and seafloor. There is a maximum value at the source depth and a minimum value at the source symmetrical depth. The amplitude of $S_2^{[f_1,f_2]}$ is close to zero. The curve of $S_3^{[f_1,f_2]}$ is symmetric with respect to $z = H/2$. At the sea surface and seafloor $S_3^{[f_1,f_2]} = 0$, with the maximum value near the zero point. Zero points are present at both the source depth and symmetrical depth, with two opposing-sign peaks on either side of the zero point.

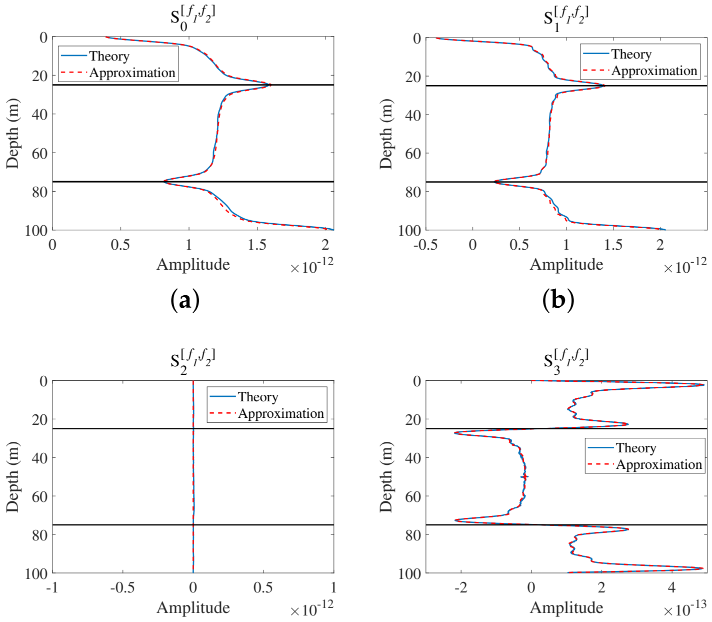

(**a**) (**b**)

(**c**) (**d**)

Figure 5. Broadband Stokes parameters depth distribution curves in an ideal solid seabed isovelocity environment: (**a**) $S_0^{[f_1,f_2]}$; (**b**) $S_1^{[f_1,f_2]}$; (**c**) $S_2^{[f_1,f_2]}$; (**d**) $S_3^{[f_1,f_2]}$.

Subsequently, we examine the depth distribution law of the polarization in a Pekeris waveguide. The simulation involves a water depth of 100 m, a water sound speed of 1500 m/s, an elastic half-space seafloor with a density of 1.5 g/cm^3, and a compression wave speed of 1800 m/s. Here, f_{c1} is set to 7 Hz.

Figure 6 presents the depth distribution curves of the broadband Stokes parameters in a Pekeris waveguide. Despite alterations in seafloor parameters, the theoretical and approximate values remain closely aligned. However, the depth distribution law of the broadband Stokes parameters changes. For $S_1^{[f_1,f_2]}$, there is no maximum value at the seafloor, and the peak at the source symmetrical depth shifts downwards. The depth distribution curve of $S_3^{[f_1,f_2]}$ becomes asymmetrical, with the lowest point now at the seafloor and the zero point at the symmetrical source depth transitioning into a peak. These changes stem from variations in seafloor parameters, affecting the modal depth functions, rendering Equation (29) ineffective. Subsequent simulation endeavors delve into exploring the impact of environmental and source parameters on the depth distribution law of polarization in a Pekeris waveguide.

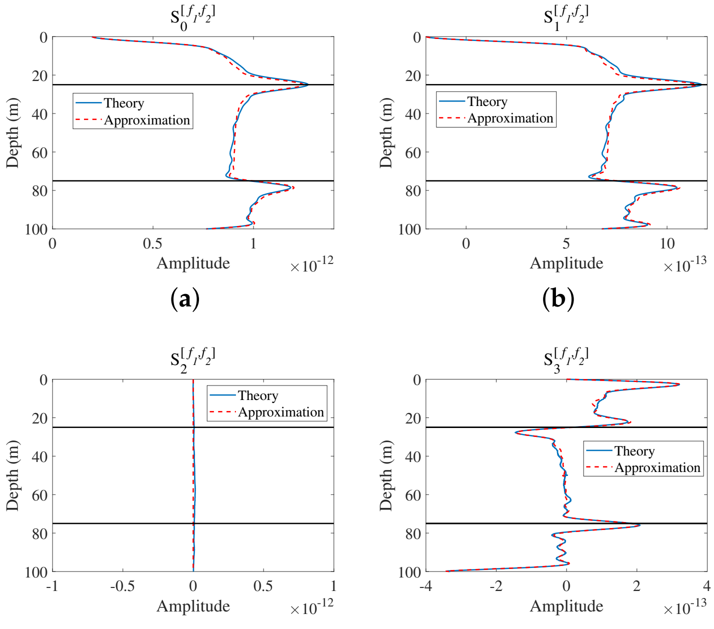

(**a**) (**b**) (**c**) (**d**)

Figure 6. Broadband Stokes parameters depth distribution curves in a Pekeris waveguide: (**a**) $S_0^{[f_1,f_2]}$; (**b**) $S_1^{[f_1,f_2]}$; (**c**) $S_2^{[f_1,f_2]}$; (**d**) $S_3^{[f_1,f_2]}$.

The results shown in Figure 6 are normalized using Equation (46), which eliminates the influence of the horizontal range r. Analysis of Figure 7 reveals that the normalized depth distribution curves of the broadband Stokes parameters follow a similar trajectory to the non-normalized curves. Since the approximate values of $S_2^{[f_1,f_2]}$ and $s_2^{[f_1,f_2]}$ are close to zero, no further analysis of $S_2^{[f_1,f_2]}$ and $s_2^{[f_1,f_2]}$ is performed.

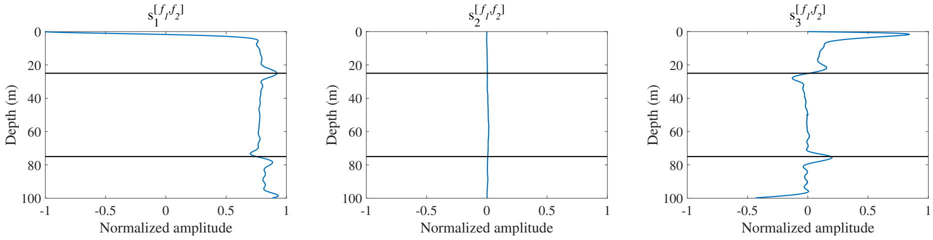

(**a**) (**b**) (**c**)

Figure 7. Normalized broadband Stokes parameters depth distribution curves for a Pekeris waveguide: (**a**) $s_1^{[f_1,f_2]}$, (**b**) $s_2^{[f_1,f_2]}$ and (**c**) $s_3^{[f_1,f_2]}$.

Figure 8 presents the depth-range distribution of the normalized broadband Stokes parameters. The results demonstrate that the depth distribution of the normalized broadband Stokes parameters remains unaffected by r. For ease of analysis, the normalized broadband Stokes parameters are employed in subsequent investigations. And we can see that s_1 jumps to about -1 at about 0 m. This is because, at z = 0, $\phi_n(0) = 0$ but $\varphi_n'(0) \neq 0$, as can be seen from Equation (29). It results in v_r being equal to 0 and v_z not equal to 0, leading to the calculation of s_1 as follows:

$$s_1 = \frac{S_1}{S_0} = \frac{|v_r|^2 - |v_z|^2}{|v_r|^2 + |v_z|^2} = \frac{-|v_z|^2}{|v_z|^2} = -1. \quad (47)$$

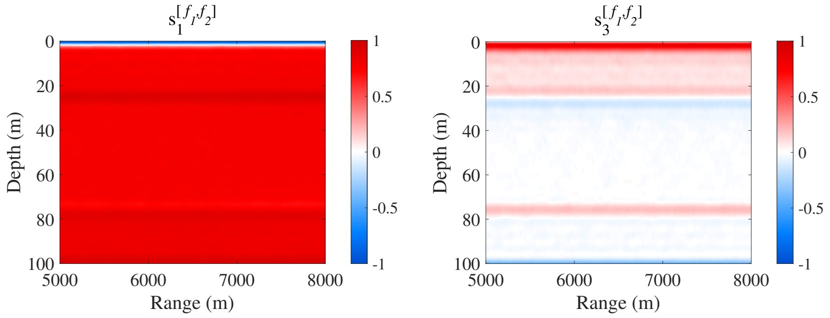

(**a**) (**b**)

Figure 8. Depth-range distribution of normalized broadband Stokes parameters for a Pekeris waveguide: (**a**) normalized broadband Stokes parameter $s_1^{[f_1,f_2]}$; (**b**) normalized broadband Stokes parameter $s_3^{[f_1,f_2]}$.

4.1. The Effect of the Sound Speed Profile

This section considers the effect of the sound speed profile on the depth distribution law of polarization. Three typical sound speed profiles are shown in Figure 9. For three sound speed profiles, f_{c1}=8Hz. The depth distribution of normalized broadband Stokes parameters for these speed profiles is illustrated in Figure 10. In three sound speed profile environments, $s_1^{[f_1,f_2]}$ maintains a peak at the source depth, while the peaks at symmetrical depths shift positions. The change of $s_3^{[f_1,f_2]}$ is similar to $s_1^{[f_1,f_2]}$: the peaks at the source depth remain stable, but those at symmetrical depths shift. According to the normal mode theory, in a non-isovelocity sound speed profile environment, the modal functions are not symmetric in the depth direction, but the peak of the superposition of propagating modes persists at the source depth [20]. This explains why the peak positions of $s_1^{[f_1,f_2]}$ and $s_3^{[f_1,f_2]}$ remain consistent at the source depth while varying at symmetrical depths.

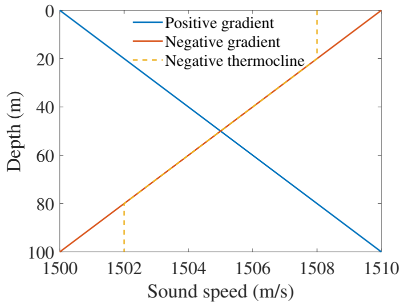

Figure 9. Sound speed profile.

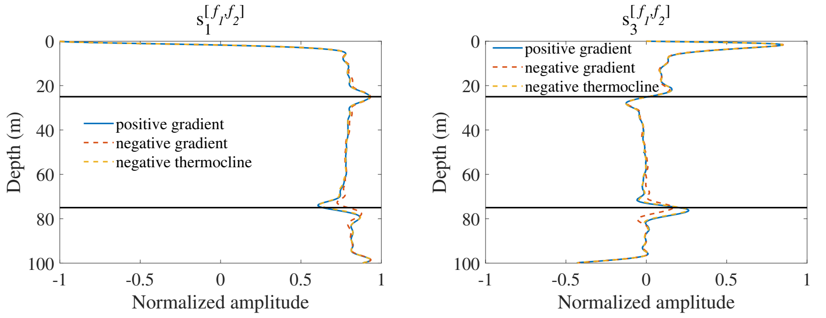

(**a**) (**b**)

Figure 10. Normalized broadband Stokes parameters depth distribution curves for different sound speed profiles:(**a**) $s_1^{[f_1,f_2]}$; (**b**) $s_3^{[f_1,f_2]}$.

4.2. The Effect of Water Depth

This section investigates the effect of water depth on the depth distribution law of polarization. Considering three Pekeris waveguides with water depths of 50 m, 100 m, and 200 m, the corresponding cutoff frequencies f_{c1} are 14 Hz, 7 Hz, and 4 Hz, respectively. The depth distribution curves of normalized broadband Stokes parameters are calculated for a source frequency band $[f_{c1}, 250\ \text{Hz}]$ at a depth of 25 m. The results are illustrated in Figure 11. Observing the figure reveals varying sharpness in the peaks of $s_1^{[f_1,f_2]}$ and $s_3^{[f_1,f_2]}$ with changes in water column depth. As the water depth increases, the amplitude of peaks increases and the width decreases. With a constant source frequency, the number of modes in the waveguide increases with the depth of the water column. As analyzed in Section 3, it is evident that the increased number of modes results in sharper peaks of the normalized broadband Stokes parameters.

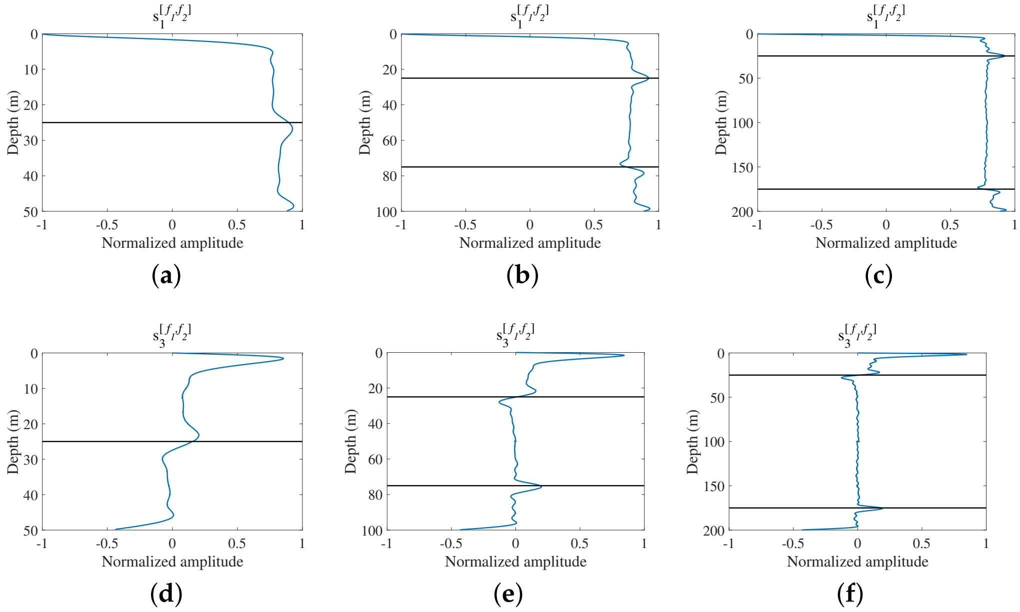

(**a**) (**b**) (**c**)

(**d**) (**e**) (**f**)

Figure 11. Normalized broadband Stokes parameters depth distribution curves for different depths of water column: (**a**) $s_1^{[f_1,f_2]}$ (depth 50 m); (**b**) $s_1^{[f_1,f_2]}$ (depth 100 m); (**c**) $s_1^{[f_1,f_2]}$ (depth 200 m); (**d**) $s_3^{[f_1,f_2]}$ (depth 50 m); (**e**) $s_3^{[f_1,f_2]}$ (depth 100 m); (**f**) $s_3^{[f_1,f_2]}$ (depth 200 m).

4.3. The Effect of Source Parameters

This section explores the impact of source parameters, encompassing source frequency and source depth. In this section, $f_{c1} = 7$ Hz. Firstly, the depth distribution of normalized broadband Stokes parameters is investigated considering three sets of frequency bands with a shared lower frequency limit of f_{c1} and upper-frequency limits of 125 Hz, 250 Hz and 500 Hz, respectively. The source depth is 25 m. The results are illustrated in Figure 12. The outcomes suggest that as bandwidth expands, the number of modes increases, leading to sharper peaks in both $s_1^{[f_1,f_2]}$ and $s_3^{[f_1,f_2]}$.

Figure 13 presents the depth distribution of normalized broadband Stokes parameters for the frequency band $[f_{c1}, 250\ \text{Hz}]$, considering different source depths. Notably, for $s_1^{[f_1,f_2]}$, a peak occurs at the source depth, while at the symmetrical depth, $s_1^{[f_1,f_2]}$ rapidly changes, forming two peaks. The behavior of $s_3^{[f_1,f_2]}$ contrasts with that of $s_1^{[f_1,f_2]}$: it undergoes rapid changes at the source depth, manifesting one positive and one negative peak, and at the symmetrical depth, it reaches a singular maximum. A unique scenario arises when $z_s = H/2$, where both $s_1^{[f_1,f_2]}$ and $s_3^{[f_1,f_2]}$ only have a single peak at $z = z_s$.

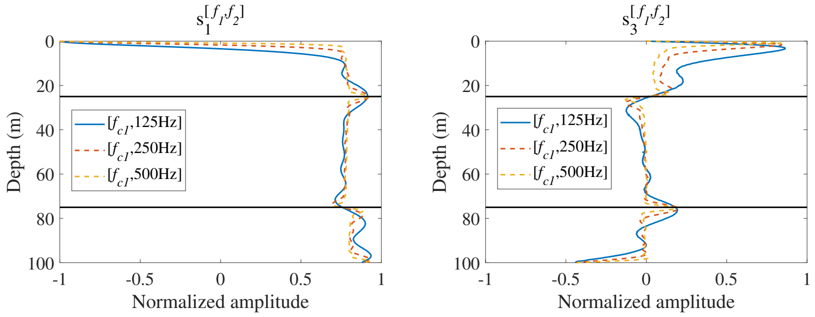

(**a**) (**b**)

Figure 12. Normalized broadband Stokes parameters depth distribution curves for different frequency ranges: (**a**) $s_1^{[f_1,f_2]}$; (**b**) $s_3^{[f_1,f_2]}$.

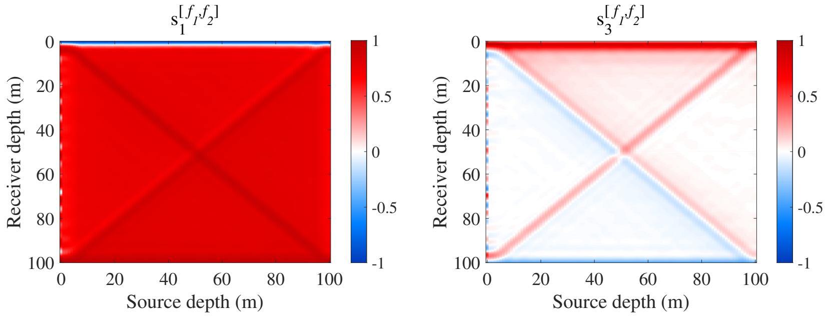

(**a**) (**b**)

Figure 13. Normalized broadband Stokes parameters depth distributions for different source depths: (**a**) $s_1^{[f_1,f_2]}$; (**b**) $s_3^{[f_1,f_2]}$.

5. Processing of OBS Experimental Data

In this section, the theoretical characteristics of the normalized broadband Stokes parameters are validated through the processing of ocean bottom seismometer (OBS) data from the RHUM-RUM experiment. This experiment involved deploying 57 OBSs over 13 months, starting from October 2012 and ending in December 2013 [21]. These OBSs were placed at depths ranging from 2500 to 5000 m, covering an extensive area of approximately 2000 × 2000 km^2 around La Réunion Island, situated between Madagascar and the neighboring South-West and Central Indian oceanic ridges [22]. These OBSs were supplied by Deutsche Geräte-Pool für Amphibische Seismologie (DEPAS), Germany, GEOMAR Helmholtz-Zentrum für Ozeanforschung Kiel (GEOMAR), Germany, and Institut National des Sciences de l'Univers—Institut de Physique du Globe de Paris (INSU-IPGP), France. Detailed information regarding the deployment, performance, and data availability of this experiment can be found in reference [23].

Based on the experimental scenario, we conduct simulations in a deep-sea waveguide with a Munk sound speed profile (as shown in Figure 14a) and a depth of 4930 m. Due to the sampling frequency of the OBS being 50 Hz, we could only analyze signals in the frequency band of 0 to 25 Hz. The calculations revealed the presence of the 87 modes in the sound field when the source frequency is 25 Hz, as illustrated in Figure 14b. It is evident that near the seabed, the amplitudes of the first 30 modes are 0, indicating that the modes with modal order greater than 30 are dominant. Therefore, in Figure 15, we present the group velocities of modes 30th to 87th within 0 to 25 Hz. It can be observed that the group velocities of distinct modes do not intersect, aligning with the assumption mandated by the non-stationary phase approximation detailed in Section 2.3. Given the above analysis, even though the OBS was positioned on the seabed in the deep sea, we believe that these data can be utilized to validate the effectiveness of the non-stationary phase approximation and the range-independence of the normalized broadband Stokes parameters.

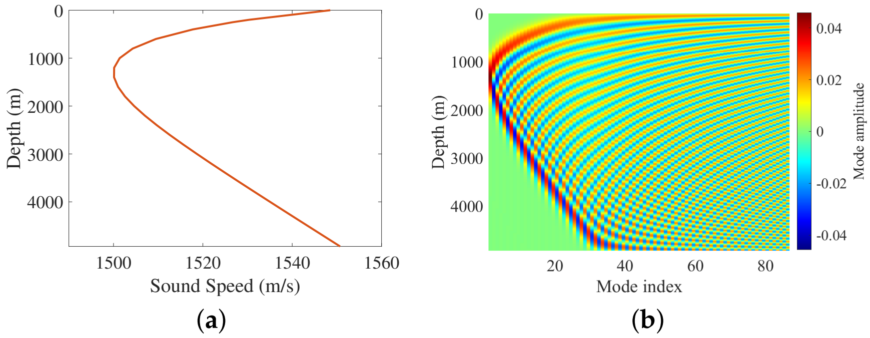

Figure 14. Simulation based on experimental conditions: (**a**) Munk sound speed profile and (**b**) corresponding distribution of mode amplitudes.

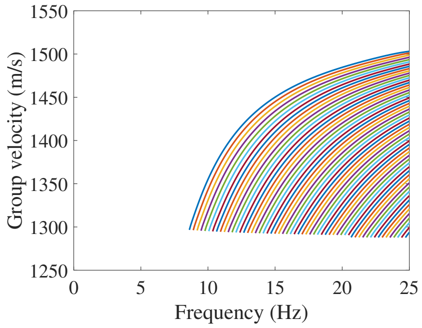

Figure 15. Group velocities of 30th to 87th modes.

To verify the theoretical law of the normalized broadband Stokes parameters, data needs to be chosen from the period when a ship passed. Analysis of AIS data reveals that a ship passed close to the RR03 station from 21:33, 28 November 2012 to 00:15, 29 November 2012. Therefore, OBS data from the RR03 station during this period are chosen for processing. The research station RR03 was situated at a depth of 4340 m, approximately 200 km west of Réunion Island. It was positioned on a flat floor that was overlaid with sediments. The cepstrogram of the OBS pressure channel during this period is shown in Figure 16, where the presence of distinct stripes indicates the passage of nearby ship [22]. Figure 17 gives a sketch of the azimuth measured, where the angle α represents the azimuth angle between the ship and the OBS, and presents the target azimuth results obtained by calculating the data from two orthogonal horizontal channels v_x and v_y. Based on the target azimuth, the v_x and v_y data can be combined to form the horizontal particle velocity v_r. The time-frequency representations of v_r and v_z are shown in Figure 18, the reference velocity is taken by the velocity in 1m depth when we calculate the spectrogram.

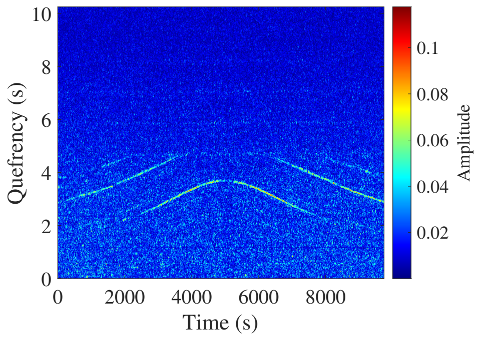

Figure 16. Cepstrogram of pressure channel.

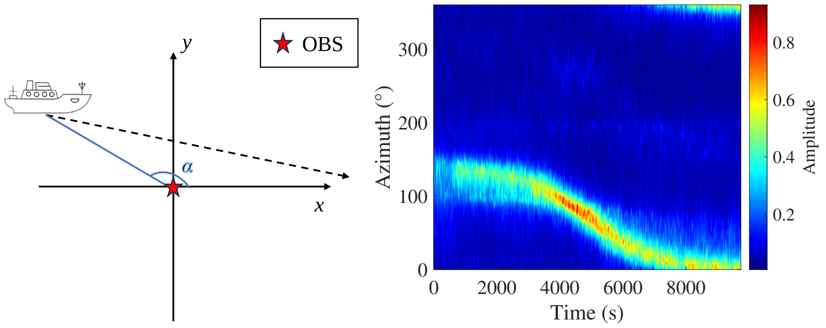

(**a**) (**b**)

Figure 17. Azimuthal detection at station RR03: (**a**) a sketch of the azimuth measured and (**b**) target azimuth results.

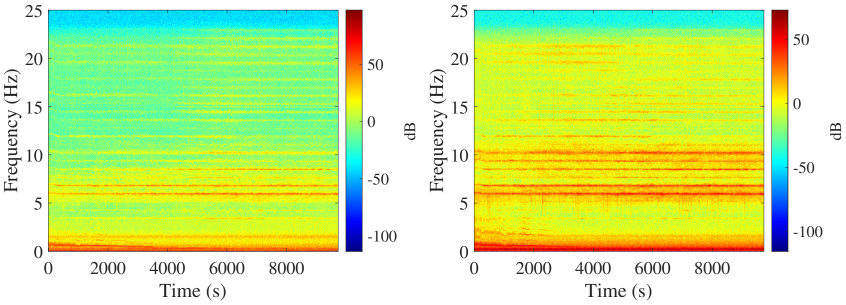

(**a**) (**b**)

Figure 18. Spectrogram of the particle velocity: (**a**) horizontal particle velocity v_r and (**b**) vertical particle velocity v_z.

Figure 19 depicts the temporal variations in the normalized broadband Stokes parameters. From the processing results, it can be seen that the value of $s_1^{[f_1,f_2]}$ is close to 1, while the values of $s_2^{[f_1,f_2]}$ and $s_3^{[f_1,f_2]}$ are close to 0. The value of $s_2^{[f_1,f_2]}$ remains approximately zero, indicating that broadband integration can effectively reduce the cross term to approach zero as long as the assumptions in Section 2.3 are satisfied. This validates the effectiveness of the non-stationary phase approximation. Finally, although the ship's position changes over time, the values of $s_1^{[f_1,f_2]}$, $s_2^{[f_1,f_2]}$ and $s_3^{[f_1,f_2]}$ exhibit only minor variation over time. It verifies the range-independent property of the normalized broadband Stokes parameters.

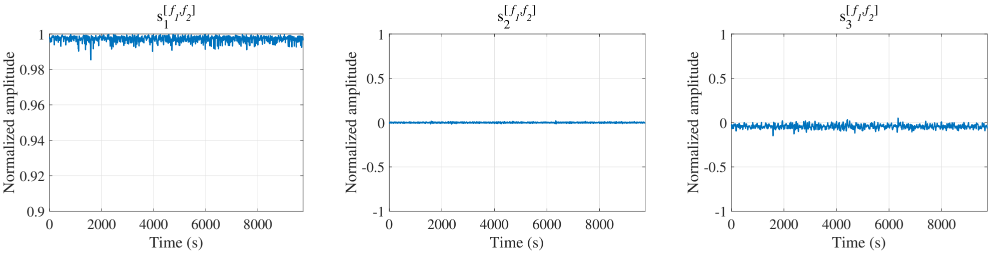

(**a**) (**b**) (**c**)

Figure 19. Time-varying curves of the normalized broadband Stokes parameters: (**a**) $s_1^{[f_1,f_2]}$; (**b**) $s_2^{[f_1,f_2]}$; (**c**) $s_3^{[f_1,f_2]}$.

6. Conclusions

This study proposes the broadband Stokes parameters based on the Stokes parameters of vector acoustic field. On this basis, the theoretical expressions for the depth distribution of polarization in an ideal isovelocity waveguide are derived. Then, the normalized broadband Stokes parameters are used to analyze the effect of environmental and source parameters on the depth distribution law of polarization. Additionally, the range-independent property of normalized broadband Stokes parameters is validated through experimental data. The conclusions are as follows:

- The polarization of the broadband source signal field shows notable variations at the sea surface, seafloor, source depth, and symmetric depth. The normalized broadband Stokes parameters, $s_1^{[f_1,f_2]}$ and $s_3^{[f_1,f_2]}$, display peaks at these locations. Conversely, $s_2^{[f_1,f_2]}$ suggests minimal linear polarization in the 45° direction across different depths. The polarization state at each depth is determined by the horizontal linear and circular polarization components;
- As the source frequency and the water depth increase, the number of modes is also increased, leading to an increase in the amplitude and a decrease in the width of peaks. The sound speed profile affects the symmetry of the modal functions, causing changes in the amplitudes and positions of peaks of the normalized broadband Stokes parameters at the source symmetric depth in a non-isovelocity environment;
- The normalized broadband Stokes parameters show a characteristic that depends only on depth and environmental factors, making them promising for estimating target depth.

Due to limitations in conditions, the experimental data only verifies a portion of the law. Our next research step involves conducting a dedicated sea trial to validate more relevant laws. Additionally, we consider exploring the application of polarization in underwater source localization.

Author Contributions: Conceptualization, Y.W.; methodology, Y.W.; software, Y.W.; validation, Y.W.; formal analysis, Y.W.; investigation, Y.W.; resources, C.S.; data curation, Y.W.; writing—original draft preparation, Y.W.; writing—review and editing, C.S.; visualization, Y.W.; supervision, C.S.; project administration, C.S.; funding acquisition, C.S. All authors have read and agreed to the published version of the manuscript.

Funding: This research was supported by National Natural Science Foundation of China Grant No. 11534009 and the Fundamental Research Funds for the Central Universities (G2024KY0604).

Institutional Review Board Statement: Not applicable.

Informed Consent Statement: Not applicable.

Data Availability Statement: The RHUM-RUM dataset used in this study is publicly available from the RESIF data centre (http://seismology.resif.fr, https://doi.org/10.15778/RESIF.YV2011, 30 April 2024). The RHUM-RUM dataset (https://www.fdsn.org/networks/detail/YV_2011/, 30 April 2024) has been assigned the FDSN network code YV and is hosted and freely accessible at the French RESIF data centre (http://seismology.resif.fr, 30 April 2024).

Acknowledgments: RHUM-RUM was funded by Agence Nationale de la Recherche (ANR) in France (project ANR-11-BS56-0013), and by Deutsche Forschungsgemeinschaft (DFG) in Germany (Grant Nos. SI1538/2-1 and SI1538/4-1). We express our gratitude to Deutsche Geräte-Pool für Amphibische Seismologie (DEPAS), Germany, GEOMAR Helmholtz-Zentrum für Ozeanforschung Kiel (GEOMAR), Germany, and Institut National des Sciences de l'Univers–Institut de Physique du Globe de Paris (INSU-IPGP), France, for supplying the ocean-bottom seismometers. The codes used to explore OBS datasets, publicly available at (https://github.com/atrabattoni/obsea, 30 April 2024). The authors also would like to thank the support of the National Natural Science Foundation of China (Grant No. 11534009) and the Fundamental Research Funds for the Central Universities (G2024KY0604).

Conflicts of Interest: The authors declare no conflicts of interest.

References

1. Long, Y.; Ren, J.; Chen, H. Intrinsic spin of elastic waves. *Proc. Natl. Acad. Sci. USA* **2018**, *115*, 9951–9955. [CrossRef]
2. Shi, C.; Zhao, R.; Long, Y.; Yang, S.; Wang, Y.; Chen, H.; Ren, J.; Zhang, X. Observation of acoustic spin. *Natl. Sci. Rev.* **2019**, *6*, 707–712. [CrossRef] [PubMed]
3. Li, J.F.; Pascal, J.C.; Carles, C. Energy fields of partially coherent sources. *J. Acoust. Soc. Am.* **1998**, *103*, 962–972. [CrossRef]
4. Bliokh, K.Y.; Nori, F. Transverse spin and surface waves in acoustic metamaterials. *Phys. Rev. B* **2019**, *99*, 020301. [CrossRef]

5. Long, Y.; Ge, H.; Zhang, D.; Xu, X.; Ren, J.; Lu, M.H.; Bao, M.; Chen, H.; Chen, Y.F. Symmetry selective directionality in near-field acoustics. *Natl. Sci. Rev.* **2020**, *7*, 1024–1035. [CrossRef]
6. Long, Y.; Zhang, D.; Yang, C.; Ge, J.; Chen, H.; Ren, J. Realization of acoustic spin transport in metasurface waveguides. *Nat. Commun.* **2020**, *11*, 4716. [CrossRef]
7. Shchurov, V.A.; Kuleshov, V.P.; Cherkasov, A.V. Vortex properties of the acoustic intensity vector in a shallow sea. *Acoust. Phys.* **2011**, *57*, 851–856. [CrossRef]
8. D'Spain, G.L.; Hodgkiss, W.S. The polarization of acoustic particle motion in the ocean. *J. Acoust. Soc. Am.* **1991**, *90*, 2300. [CrossRef]
9. Dall'Osto, D.R.; Dahl, P.H. Elliptical acoustic particle motion in underwater waveguides. *J. Acoust. Soc. Am.* **2013**, *134*, 109–118. [CrossRef] [PubMed]
10. Dahl, P.H.; Dall'Osto, D.R. Vector Acoustic Analysis of Time-Separated Modal Arrivals From Explosive Sound Sources During the 2017 Seabed Characterization Experiment. *IEEE J. Ocean. Eng.* **2020**, *45*, 131–143. [CrossRef]
11. Dahl, P.H.; Dall'Osto, D.R. Range-Dependent Inversion for Seabed Parameters Using Vector Acoustic Measurements of Underwater Ship Noise. *IEEE J. Ocean. Eng.* **2022**, *47*, 680–689. [CrossRef]
12. Liu, W. Model Based DOA Estimation for Acoustic Vector Sensor Array. Ph.D. Thesis, Harbin Engineering University, Harbin, China, 2014.
13. Bonnel, J.; Flamant, J.; Dall'Osto, D.R.; Le Bihan, N.; Dahl, P.H. Polarization of ocean acoustic normal modes. *J. Acoust. Soc. Am.* **2021**, *150*, 1897–1911. [CrossRef] [PubMed]
14. Born, M.; Wolf, E. *Principles of Optics: Electromagnetic Theory of Propagation, Interference and Diffraction of Light*; Publishing House of Electronics Industry: Beijing, China, 2016; pp. 20–27.
15. Dahl, P.H.; Bonnel, J. Vector acoustic and polarization properties of underwater ship noise. *J. Acoust. Soc. Am.* **2022**, *151*, 3818–3827. [CrossRef] [PubMed]
16. Dahl, P.H.; Dall'Osto, D.R.; Hodgkiss, W.S. Active intensity vortex and stagnation point singularities in a shallow underwater waveguide. *J. Acoust. Soc. Am.* **2023**, *154*, 1482–1492. [CrossRef] [PubMed]
17. Wu, D.; Zhang, L.; Wang, J.; Hu, X. Using High-Order Particle Velocity Gradient Polarization Characteristics to Detect Underwater Coherent Interference. *J. Mar. Sci. Eng.* **2023**, *11*, 1027. [CrossRef]
18. Jensen, F.B.; Kuperman, W.A.; Porter, M.B.; Schmidt, H. *Computational Ocean Acoustics*, 2nd ed.; National Defense Industry Press: Beijing, China, 2017.
19. Flamant, J.; Bonnel, J. Broadband properties of potential and kinetic energies in an oceanic waveguide. *J. Acoust. Soc. Am.* **2023**, *153*, 3012. [CrossRef] [PubMed]
20. Zhang, H.G.; Xie, J.H.; Liu, J.Q.; Gong, L.J; Li, Z. The depth distribution characteristics of particle velocity field intensity in shallow sea. *J. Shanghai Jiaotong Univ.* **2023**, *58*, 995–1005.
21. Tsekhmistrenko, M.; Sigloch, K.; Hosseini, K.; Barruol, G. A tree of Indo-African mantle plumes imaged by seismic tomography. *Nat. Geosci.* **2021**, *14*, 612–619. [CrossRef]
22. Trabattoni, A.; Barruol, G.; Dréo, R.; Boudraa, A. Ship detection and tracking from single ocean-bottom seismic and hydroacoustic stations. *J. Acoust. Soc. Am.* **2023**, *153*, 260–273. [CrossRef] [PubMed]
23. Stähler, S.C.; Sigloch, K.; Hosseini, K.; Crawford, W.C.; Barruol, G.; Schmidt-Aursch, M.C.; Tsekhmistrenko, M.; Scholz, J.-R.; Mazzullo, A. Performance report of the RHUM-RUM ocean bottom seismometer network around La Réunion, western Indian Ocean. *Adv. Geosci.* **2016**, *41*, 43–63. [CrossRef]